Nanoscale

PAPER

View Article Online
View Journal | View Issue

Cite this: *Nanoscale*, 2024, **16**, 6278

An enhanced electrocatalytic oxygen evolution reaction by the photothermal effect and its induced micro-electric field†

Feng Duan,[a] Qian Zou,[a] Junzhe Li,[a] Xiaozhi Yuan,[a] Xun Cui,[c] Chuan Jing,[d] Shengrong Tao,[d] Xijun Wei,*[a] Huichao He*[b] and Yingze Song*[a]

Promoting better thermodynamics and kinetics of electrocatalysts is key to achieving an efficient electrocatalytic oxygen evolution reaction (OER). Utilizing the photothermal effect and micro-electric field of electrocatalysts is a promising approach to promote the sluggish OER. Herein, to reveal the relationship of the photothermal effect and its induced micro-electric field with OER performance, NiS_x coupled NiFe $(OH)_y$ on nickel foam (NiS_x@NiFe$(OH)_y$/NF) is synthesized and subjected to the OER under near-infrared (NIR) light. Owing to the photothermal effect and its induced micro-electric field, the OER performance of NiS_x@NiFe$(OH)_y$/NF is significantly enhanced. Compared with no NIR light irradiation, the overpotential at 50 mA cm^{-2} and the Tafel slope of NiS_x@NiFe$(OH)_y$/NF under NIR light irradiation were 234.1 mV and 38.0 mV dec^{-1}, which were lower by 12.4 mV and 7.1 mV dec^{-1}, and it exhibited stable operation at 1.6 V *vs.* RHE for 8 h with 99% activity maintained. This work presents a novel inspiration to understand the photothermal effect-enhanced electrocatalytic OER.

Received 12th January 2024,
Accepted 20th February 2024

DOI: 10.1039/d4nr00170b

rsc.li/nanoscale

1. Introduction

Hydrogen energy is one of the clean and non-polluting energies with huge potential to replace traditional fossil energy.[1–5] Alkaline water electrolysis is an economical method for clean hydrogen generation.[6–9] However, hydrogen production by alkaline water electrolysis is generally limited by the inherent thermodynamics and sluggish kinetics resulting from the slow four-electron water oxidation process at the anode ($4OH^- \rightarrow 2H_2O + O_2 + 4e^-$).[10–12] To achieve an efficient OER, many materials are being utilized as electrocatalysts, such as noble metal-based OER electrocatalysts[13,14] (*e.g.*, RuO_2 and IrO_2) and transition metal-based OER electrocatalysts[15–20] (*e.g.*, oxides, hydroxide, carbides, phosphides, sulfides, nitrides and polymers). Among them, Ni–Fe-based hydroxide catalysts have exhibited excellent OER activity in alkaline electrolytes due to the bimetallic synergistic effect of Ni and Fe as well as the optimized electronic structures resulting from the rearrangement of the metal atoms.[21–23] However, the OER performance of Ni–Fe-based hydroxide is strongly limited by the active sites at the edges and weak conductivity.[24,25] In addition, a proper ratio of Ni^{2+}/Ni^{3+} is crucial for improving the OER properties of Ni–Fe based hydroxide electrocatalysts.[26]

As a classical nonhomogeneous reaction, the electrocatalytic OER is known to contain both thermodynamic and kinetic processes.[27,28] In recent years, amorphous electrocatalysts for the electrocatalytic OER have been widely reported to optimize the adsorption and activation of H_2O and OH^-, the formation of intermediates (O*, OH*, and OOH*) and generation and desorption of O_2, which provided a new strategy to enhance the OER activity of Ni–Fe hydroxide.[29–32] Furthermore, a previous report has shown that the flat band voltage of Ni–Fe hydroxide is around 0.06 V *vs.* RHE.[33] Thus, according to the heterojunction theory, coupling of materials with different flat-band potentials with Ni–Fe hydroxide can optimize its intrinsic electronic structure and lead to rebalancing of the Fermi level.[34] In our previous report, Ni–sulfide (NiS_x) coupled with Co_3O_4 can format a more advantageous electronic structure, and the flat-band potential of nickel sulfides has been reported to be around −0.64 V *vs.* RHE.[35,36] Therefore, it can be assumed that NiS_x/NiFe hydroxide would

[a]*State Key Laboratory of Environment-Friendly Energy Materials, School of Materials and Chemistry, Engineering Research Center of Biomass Materials, Ministry of Education, Southwest University of Science and Technology, Mianyang 621010, P. R. China. E-mail: xijunwei1992@swust.edu.cn, yzsong@swust.edu.cn*
[b]*Institute of Environmental Energy Materials and Intelligent Devices, School of Metallurgy and Materials Engineering, Chongqing University of Science and Technology, Chongqing 401331, P. R. China. E-mail: hehuichao@cqust.edu.cn*
[c]*State Key Laboratory of New Textile Materials and Advanced Processing Technologies, Wuhan Textile University, Wuhan 430200, P. R. China*
[d]*College of Science, Chongqing University of Posts and Telecommunications, Chongqing 400065, P. R. China*
† Electronic supplementary information (ESI) available. See DOI: https://doi.org/10.1039/d4nr00170b

facilitate the formation of more suitable Ni^{2+}/Ni^{3+} ratios, thus driving an efficient OER.

In addition to modifying the electronic structure of electrocatalysts, achieving enhanced strategies for electrocatalysis using the temperature field generated by the photothermal effect has become an interesting topic in recent years.[37–41] From the Arrhenius law $\left(k = A\exp\left(-\frac{E_a}{RT}\right)\right)$, the catalytic reaction temperature (T) could be known to have a vital influence on the reaction rate (k).[42] Electrodes with photo-thermal conversion capability are able to directly utilize energy from renewable solar energy and be heated, which provides a novel strategy to achieve an efficient and economical electrocatalytic reaction. Furthermore, previous experiments as well as simulation studies proved that the construction of semiconductor heterostructures induces the equilibrium of Fermi energy levels, which accelerates electron transfer and creates a micro-electric field induced by photothermal effects.[39,43] The micro-electric field can effectively change the adsorption and desorption of reactive substances on the electrocatalyst surface, thus effectively improving the reaction kinetics. Notably, the photothermal response of NiS_x in the near-infrared region has been extensively proved.[44,45] Thus, these advantages indicated that NiS_x/NiFe hydroxide heterostructures can effectively drive a photothermal OER.

Herein, in order to unravel the influence of the photothermal effect and its induced micro-electric field on the thermodynamics and kinetics of the OER, amorphous NiS_x@NiFe$(OH)_y$/NF was prepared for a highly efficient OER under NIR light irradiation. Due to the photothermal effect and the induced micro-electric field, the OER performance of NiS_x@NiFe$(OH)_y$/NF was significantly enhanced. Notably, compared with no NIR light irradiation, the overpotential at 50 mA cm^{-2} and the Tafel slope of NiS_x@NiFe$(OH)_y$/NF under NIR light irradiation were 234.1 mV and 38.0 mV dec^{-1}, which were lower by 12.4 mV and 7.1 mV dec^{-1}, respectively. Furthermore, NiS_x@NiFe$(OH)_y$/NF under NIR irradiation was able to run stably at 1.6 V *vs.* RHE for 8 h with 99% activity maintained. This work provides novel understanding with beneficial reference towards the enhancement of the water oxidation reaction by the photothermal effect.

2. Experimental section

2.1 Materials preparation

2.1.1 Fabrication of NiFe$(OH)_y$/NF and NiFe$(OH)_y$/FTO. NiFe$(OH)_y$ was grown on nickel foam (NF) using an electrodeposition process. To begin with, a NF (1.0 × 2.0 cm) substrate was immersed in 1.0 M hydrochloric acid for 30 min, and then washed several times sequentially with deionised water and ethanol. The electrodeposition process of NiFe$(OH)_y$ on NF was conducted on a three-electrode system using a CHI 760E workstation. The pre-treated NF was employed directly as the working electrode. An Ag/AgCl electrode and a graphite rod (99%) electrode were used as the reference and counter electrodes, respectively. The composition of the electrolyte was an aqueous solution containing 0.05 M $Ni(NO_3)_2{\cdot}6H_2O$ and 0.05 M $Fe(NO_3)_3{\cdot}9H_2O$. The electrodeposition of NiFe$(OH)_y$/NF was performed at a potential of −1.0 V *vs.* Ag/AgCl for 100 s. After the electrodeposition, the as-prepared NiFe$(OH)_y$/NF was cleaned several times with deionized water and dried at 60 °C for 6 h in a vacuum oven. For comparison, NiFe$(OH)_y$ was synthesized with the same electrodeposition method using fluorine-doped tin oxide glass (FTO) as the working electrode. The NiFe$(OH)_y$ sample was obtained on NF and FTO with a loading of 1.0 mg cm^{-2}.

2.1.2 Fabrication of NiS_x@NiFe$(OH)_y$/NF and NiS_x@NiFe$(OH)_y$/FTO. The NiS_x@NiFe$(OH)_y$/NF electrode was synthesized on the as-prepared NiFe$(OH)_y$/NF electrode by the electrodeposition method. The electrodeposition process of NiS_x on NiFe$(OH)_y$/NF was conducted on a three-electrode system using a CHI 760E workstation. The prepared NiFe$(OH)_y$/NF was directly used as the working electrode. An Ag/AgCl electrode and a graphite rod (99%) electrode were used as the reference and counter electrodes, respectively. The composition of the electrolyte was an aqueous solution containing 0.025 M $Ni(NO_3)_2{\cdot}6H_2O$ and 0.75 M thiourea. The electrodeposition of NiS_x on NiFe$(OH)_y$/NF was conducted by cyclic voltammetry (CV) in a potential window of −1.2 to 0.2 V *vs.* Ag/AgCl. CV was performed at a scan rate of 10 mV s^{-1} for two cycles. After electrodeposition, the as-prepared NiS_x@NiFe$(OH)_y$/NF was washed with deionized water and dried at 60 °C for 6 h in a vacuum oven. For comparison, NiS_x@NiFe$(OH)_y$ was synthesized with the above electrodeposition method using NiFe$(OH)_y$/FTO as the working electrode. The NiS_x@NiFe$(OH)_y$ sample was obtained on NF and FTO with a loading of 1.3 mg cm^{-2}. In addition, NiS_x/NF was prepared using an electrodeposition method under the same conditions, where NiFe$(OH)_y$/FTO was replaced with NF as the working electrode. NiS_x was obtained on NF loaded at 0.3 mg cm^{-2}.

2.2 Characterization studies

An X-ray diffractometer was used (XRD, PANalytical X'pert PRO) to examine the crystal structures of samples. The morphologies and elemental micrographs of samples were analyzed using a scanning electron microscope (SEM, Zeiss SUPRA 55VP) equipped with an energy-dispersive X-ray (EDS) analyzer. Transmission electron microscopy (TEM, FEI Talos F200X) recorded the microstructures of samples. X-ray photoelectron spectroscopy (XPS) of the samples was carried out using a Thermo Scientific K-Alpha spectrometer. The water contact angle of samples was tested and documented using a Kruss K100 surface tension meter.

2.3 Electrochemical measurements

All the electrochemical properties were determined using a standard three-electrode quartz cell using a CHI 760E workstation. The fabricated electrodes were used as the working electrode. A graphite rod and a standard Hg/HgO electrode were applied as the counter electrode and reference electrode, respectively. The composition of the electrolyte was an aqueous solution containing 1.0 M KOH. Before electro-

chemical measurements, 5 cycles of CV activation of working electrodes at a scan rate of 2 mV s^{-1} within a potential window of 1.0 V to 1.8 V *vs.* RHE were performed. Linear sweep voltammetry (LSV) was performed at a scanning rate of 2 mV s^{-1}. The tested potentials were transformed into the potentials *vs.* RHE using the Nernst equation for manual *iR*-compensation:

$$E_{RHE} = E_{Hg/HgO} + E^{\Theta}_{Hg/HgO} + 0.059\ pH - IR_s, \quad (1)$$

where $E^{\Theta}_{Hg/HgO}$ = 0.098 V at room temperature (25 ± 0.5 °C), pH is the pH value of 1.0 M KOH electrolyte (pH = 13.71), I is the current density (J), and R_s is the solution resistance. Electrochemical impedance spectroscopy (EIS) was performed in a frequency scale between 0.1 and 10^5 Hz with an AC voltage amplitude of 5 mV. Equivalent circuits were fitted for the recorded EIS data using ZView software. The electrochemically active surface area (ECSA) of all samples was obtained based on the CV test performed using the double layer capacitance method (C_{dl}). The CV curves of samples were tested in the non-faradaic potential area with scanning rates of 10, 20, 30, 40, and 50 mV s^{-1}. Subsequently, a linear relationship of the anodic–cathodic current density (ΔJ) and the scan rate (ν) was fitted. The C_{dl} value was calculated using half the slope value obtained from the ΔJ *vs.* scan rate curve. All the ECSA values were derived from the C_{dl} value and the following formula:[46]

$$ECSA = C_{dl}/C_s, \quad (2)$$

where C_s is the capacitance of NF.

The oxygen generation rate of NiS_x@$NiFe(OH)_y$/NF was calculated from the Faraday law and the precondition that the electrode current efficiency is 100%:[47,48]

$$Q = nZF, \quad (3)$$

$$N_{O_2} = n \times 1000/t, \quad (4)$$

where Q is the overall charge on the electrode that was measured on an electrochemical workstation, n is the mass of oxygen, Z is the number of electrons transferred (Z = 4), F is the Faraday constant (96 485 C mol^{-1}), N_{O_2} is the rate of oxygen formation (mmol h^{-1}), and t is the time of the reaction (h).

The turnover frequency (TOF) is calculated according to the following formula:

$$TOF = \frac{J \times A}{Z \times F \times n} \quad (5)$$

where J is the value of the catalytic current, A is the geometric area of the electrode (1 cm^2), Z is the electron transfer number, F is the Faraday constant (96 485 C mol^{-1}), and n is the number of catalytically active sites (mol cm^{-2}).

2.4 Photothermal measurements

Near infrared transformation characteristics of the electrodes in the electrolyte were evaluated using NIR light (wavelength: 808 nm, optical watt density: 2 W cm^{-2}). A water recirculation device was used to avoid the increase in electrolyte temperature under prolonged testing (Fig. S11†). Thermal imaging pictures were recorded using an IR camera (C5, FLIR Systems, Inc., USA), and the temperature of the electrode surfaces illuminated by NIR was examined.

3. Results and discussion

3.1 Characterization of NiS_x@$NiFe(OH)_y$/NF

Fig. 1a illustrates the preparation of NiS_x@$NiFe(OH)_y$/NF by a two-step electrodeposition method, and the image of the resulting samples is shown in Fig. S1.† Fig. 1b exhibits the SEM image of NiS_x@$NiFe(OH)_y$/NF. The corresponding EDS mapping of NiS_x@$NiFe(OH)_y$/NF is shown in Fig. S2,† which demonstrates the existence of the Ni, Fe, S and O elements. Compared to the SEM image of single $NiFe(OH)_y$/NF and NiS_x/NF (Fig. 1c and Fig. S3†), NiS_x@$NiFe(OH)_y$/NF has a distinct flocculent presence on the surface of $NiFe(OH)_y$/NF. Fig. 1d shows the XRD patterns of NiS_x@$NiFe(OH)_y$/NF, $NiFe(OH)_y$/NF, NiS_x/NF and bare NF. Notably, only the diffraction peaks (44.5°, 51.6° and 76.1°) of NF were observed in all samples. In order to exclude the effect of the substrate, the XRD of NiS_x@$NiFe(OH)_y$/NF deposited on the FTO substrate was tested. Similarly, no diffraction peaks other than those of the substrate were seen (Fig. S4†), suggesting that NiS_x and $NiFe(OH)_y$/NF have weak crystallinity. To further detect the microstructure and morphological details, NiS_x@$NiFe(OH)_y$/NF was selected for TEM and high-resolution TEM (HRTEM) character-

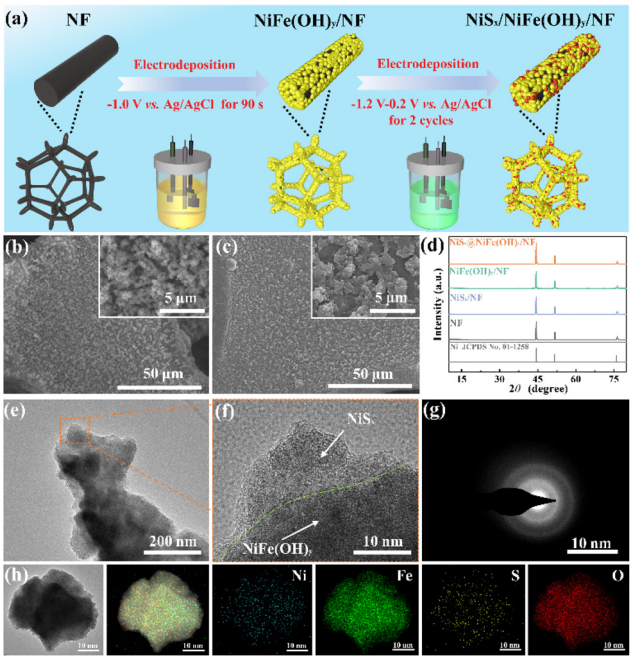

Fig. 1 (a) Schematic diagram of the synthesis route for NiS_x@$NiFe(OH)_y$/NF. SEM images of (b) NiS_x@$NiFe(OH)_y$/NF and (c) $NiFe(OH)_y$/NF. (d) XRD patterns of NiS_x@$NiFe(OH)_y$/NF, $NiFe(OH)_y$/NF, NiS_x/NF and NF. (e) TEM image, (f) high-resolution TEM image, and (g) SAED pattern of NiS_x@$NiFe(OH)_y$ in NiS_x@$NiFe(OH)_y$/NF. (h) HAADF-TEM image and the corresponding STEM-EDS elemental mapping images of NiS_x@$NiFe(OH)_y$ in NiS_x@$NiFe(OH)_y$/NF.

ization. Fig. 1e shows the TEM image of NiS_x@NiFe$(OH)_y$ in the NiS_x@NiFe$(OH)_y$/NF sample. The HRTEM image of NiS_x@NiFe$(OH)_y$ is shown in Fig. 1f, which clearly exhibits weak crystallinity with no typical lattices of NiS_x and NiFe$(OH)_y$. Correspondingly, the absence of distinct crystalline surfaces was observed from the selected area electron diffraction (SAED) pattern (Fig. 1g).

In addition, Fig. 1h shows the STEM-EDS elemental mapping of NiS_x@NiFe$(OH)_y$, which indicates an even distribution of Ni, Fe, O and S elements, suggesting that NiS_x is uniformly deposited on the surface of NiFe$(OH)_y$/NF. Furthermore, NF is hydrophobic with a contact angle of 109.8°, while the prepared NiS_x@NiFe$(OH)_y$/NF surface is superhydrophilic, which enhances the affinity and osmotic hydrophilicity of the electrolyte and thus facilitates the OER process of NiS_x@NiFe$(OH)_y$/NF (Fig. S5†). From the above investigation, it was seen that NiS_x@NiFe$(OH)_y$/NF is an amorphous heterostructure. As discussed later, this structure has a more suitable electronic structure, which is one of the reasons for its enhanced OER activity.

3.2 OER activity and kinetics of NiS_x@NiFe$(OH)_y$/NF

Fig. 2a shows the LSV curves of NF, NiS_x/NF, NiFe$(OH)_y$/NF, and NiS_x@NiFe$(OH)_y$/NF. Compared with bare NF, NiS_x/NF and NiFe$(OH)_y$/NF, NiS_x@NiFe$(OH)_y$/NF has a higher OER current density with an overpotential of 246.5 mV at 50 mA cm^{-2}, which was superior to those of NiS_x/NF (330.4 mV) and NiFe$(OH)_y$/NF (264.1 mV) (Fig. 2b). In addition, NiS_x@NiFe$(OH)_y$/NF exhibited a Tafel slope of 45.1 mV dec^{-1}, which was lower than those of NiS_x/NF (86.1 mV dec^{-1}) and NiFe$(OH)_y$/NF (50.3 mV dec^{-1}), suggesting the enhanced reaction kinetics of NiS_x@NiFe$(OH)_y$/NF (Fig. 2c). Notably, these Tafel slope results demonstrated that NiS_x@NiFe$(OH)_y$/NF has excellent catalytic kinetics for the OER, which is competitive compared to the reported Ni–Fe-based catalysts in recent years (Table S1†). To gain insight into the intrinsic catalytic activity of NiS_x@NiFe$(OH)_y$/NF, the EIS of samples was measured. Fig. 2d shows the EIS results of the samples at 1.6 V *vs.* RHE. Among all samples, the charge transfer resistance of the NiS_x@NiFe$(OH)_y$/NF catalyst is 0.5 Ω, which is smaller than that of NiS_x/NF (1.15 Ω) and NiFe$(OH)_y$/NF (0.61 Ω), suggesting that it possesses the best OER charge transfer capability and reaction kinetics, corresponding to the Tafel slope results. To avoid disturbances in electrochemical activity by NF substrates, NiS_x@NiFe$(OH)_y$ and NiFe$(OH)_y$ were prepared on FTO to further evaluate their activity and kinetics (NiS_x@NiFe$(OH)_y$/FTO and NiFe$(OH)_y$/FTO, Fig. S6†). As shown in Fig. S7,† the LSV and EIS results also show that NiS_x@NiFe$(OH)_y$/FTO exhibits higher OER activity and kinetics than NiFe$(OH)_y$/FTO, respectively. In order to evaluate the OER long-term stability, the *J*–*T* curves of NiS_x@NiFe$(OH)_y$/NF, NiFe$(OH)_y$/NF and NiS_x/NF were tested at 1.6 V *vs.* RHE for 24 h. As shown in Fig. 2e, NiS_x@NiFe$(OH)_y$/NF maintains 93% OER activity after 24 h, which does not change significantly compared to those of NiFe$(OH)_y$/NF (89%) and NiS_x/NF (88%), indicating that NiS_x@NiFe$(OH)_y$/NF has excellent OER stability. Based on the aforementioned studies, it can be seen that NiS_x@NiFe$(OH)_y$/NF exhibits better OER activity and kinetics and maintains desirable long-term stability compared to NiFe$(OH)_y$/NF and NiS_x/NF.

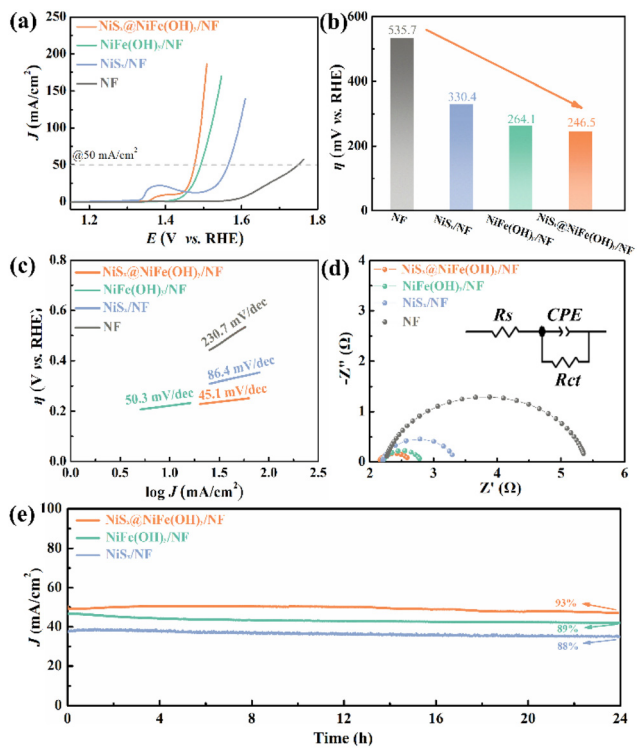

Fig. 2 OER performance of NiS_x/NF, NiFe$(OH)_y$/NF and NiS_x@NiFe$(OH)_y$/NF: (a) LSV curves, (b) overpotential values at 50 mA cm^{-2}, (c) Tafel slopes calculated using the LSV curves, (d) EIS spectra and (e) *J*–*T* curves at 1.6 V *vs.* RHE for 24 h.

To further clarify the origin of the enhanced OER activity and kinetics of NiS_x@NiFe$(OH)_y$/NF, we employed XPS to determine the interaction at the heterogeneous interface. As shown in Fig. S8,† the survey XPS shows the existence of elemental Ni, Fe, O and S in NiS_x@NiFe$(OH)_y$/NF, elemental Ni, Fe and O in NiFe$(OH)_y$/NF, and elemental Ni and S in NiS_x/NF, which is in accordance with the EDS mapping and STEM-EDS mapping results. The chemical states of NiS_x@NiFe$(OH)_y$/NF, NiFe$(OH)_y$/NF and NiS_x/NF were compared by high-resolution XPS. As shown in Fig. 3a, the binding energies of Ni^{2+} (855.1/872.8 eV) and Ni^{3+} (856.9/875.0 eV) of NiS_x@NiFe$(OH)_y$/NF were shifted between those of Ni^{2+} and Ni^{3+} in NiFe$(OH)_y$/NF and NiS_x/NF, which suggests that the interfacial interaction between NiFe$(OH)_y$/NF and NiS_x/NF resulted in the redistribution of charge at the interface. In addition, NiS_x@NiFe$(OH)_y$/NF and NiFe$(OH)_y$/NF have the same binding energies of Fe^{2+} (710.1/723.9 eV) and Fe^{3+} (713.3/727.4 eV), which suggests that there is no significant change in Fe binding energy before and after the introduction of NiS_x (Fig. S9†). Moreover, the S peak (Fig. 3b) and O peak (Fig. 3c) of NiS_x@NiFe$(OH)_y$/NF are shifted to smaller binding energies by 0.1 eV and 0.4 eV, respectively, with respect to NiFe$(OH)_y$/NF

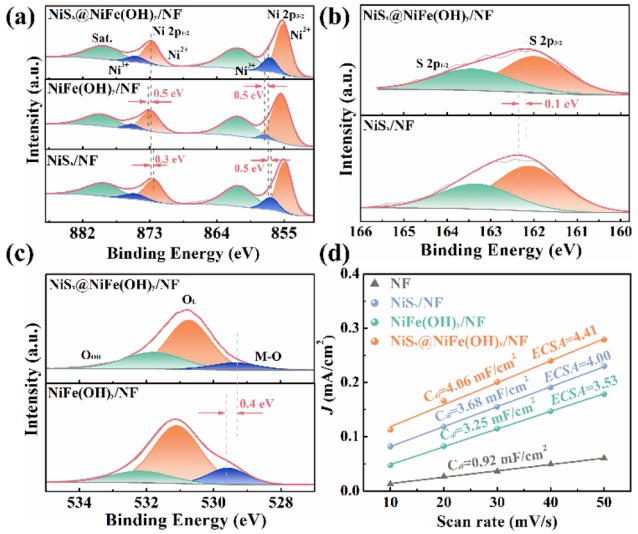

Fig. 3 High-resolution XPS comparison of (a) Ni 2p, (b) S 2p and (c) O 1s for NiS_x@$NiFe(OH)_y$/NF, $NiFe(OH)_y$/NF and NiS_x/NF. (d) ECSA values of NiS_x@$NiFe(OH)_y$/NF, $NiFe(OH)_y$/NF and NiS_x/NF.

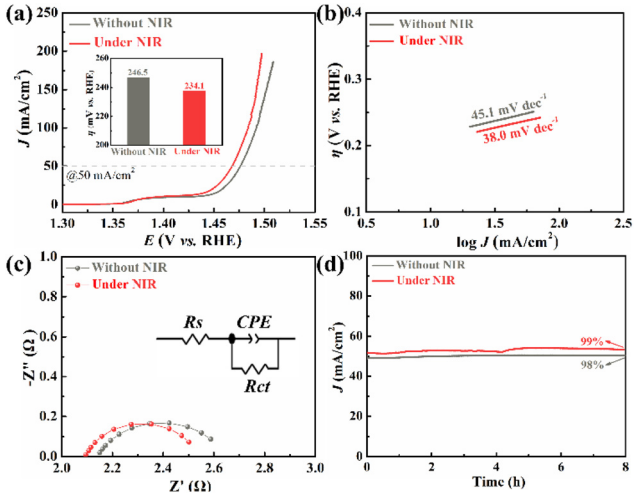

Fig. 4 OER performance of NiS_x@$NiFe(OH)_y$/NF under and without NIR light: (a) LSV curves (inset: the overpotential at 50 mA cm^{-2} of NiS_x@$NiFe(OH)_y$/NF under and without NIR light), (b) Tafel slopes derived from the LSV curves, (c) EIS spectra, and (d) *J*–*T* curves at 1.6 V *vs.* RHE for 8 h.

and NiS_x/NF, which further proves that $NiFe(OH)_y$/NF and NiS_x/NF have electron transfer at the interface of NiS_x@$NiFe(OH)_y$/NF.[49,50] Furthermore, it has been reported that small changes in the binding states of Ni can lead to the formation of increased active sites on OER electrocatalysts.[51] The larger ECSA on NiS_x@$NiFe(OH)_y$/NF (4.41) than that on NiS_x/NF (4.00) and $NiFe(OH)_y$/NF (3.53) implies that the interfacial interaction of the heterogeneous structure of NiS_x@$NiFe(OH)_y$/NF can form more electrochemically active sites (Fig. 3d and Fig. S10†), and Ni is the main active site during the OER.

3.3 OER activity and kinetics of NiS_x@$NiFe(OH)_y$/NF under NIR light irradiation

After establishing NiS_x@$NiFe(OH)_y$/NF as the electrode that has the best OER activity in this work, we further evaluated the photothermal effect of NiS_x@$NiFe(OH)_y$/NF and attempted to further enhance its OER performance. To verify the impact of the photothermal effect on the electrocatalytic OER of NiS_x@$NiFe(OH)_y$/NF, we added 808 nm light (2 W cm^{-2}) to irradiate the NiS_x@$NiFe(OH)_y$/NF sample during the OER test (NiS_x@$NiFe(OH)_y$/NF-NIR). As shown in Fig. 4a, as expected, the LSV curves show that the OER activity on NiS_x@$NiFe(OH)_y$/NF is increased under NIR light illumination, and the overpotential of NiS_x@$NiFe(OH)_y$/NF at 50 mA cm^{-2} is 234.1 mV, which is lower by 12.4 mV than that of the unirradiated NiS_x@$NiFe(OH)_y$/NF. As shown in Fig. S12,† NiS_x@$NiFe(OH)_y$/NF-NIR has a higher TOF than NiS_x@$NiFe(OH)_y$/NF, indicating that NiS_x@$NiFe(OH)_y$/NF has a higher catalytic efficiency under NIR light irradiation. Furthermore, NiS_x@$NiFe(OH)_y$/NF under NIR light exhibited a Tafel slope of only 38.0 mV dec^{-1}, which was lower than that of NiS_x@$NiFe(OH)_y$/NF without NIR light as well as those mentioned in related reports (Table S1†), suggesting the enhanced reaction kinetics (Fig. 4b). In order to understand the difference in the intrinsic catalytic activity of NiS_x@$NiFe(OH)_y$/NF under and without NIR light, the samples were subjected to EIS and ECSA measurements. As shown in Fig. 4c and Table S2,† NiS_x@$NiFe(OH)_y$/NF has lower solution resistance (R_s) under NIR light irradiation (2.10 Ω), which is probably related to the accelerated ion transport at the electrode–electrolyte interface induced by the photothermal effect. In addition, NiS_x@$NiFe(OH)_y$/NF under NIR light shows an R_{ct} value of 0.44 Ω, which is smaller than that of NiS_x@$NiFe(OH)_y$/NF without NIR light (0.50 Ω) (Table S3†). The larger ECSA on NiS_x@$NiFe(OH)_y$/NF under NIR light (5.01) than that of NiS_x/NF NiS_x@$NiFe(OH)_y$/NF without NIR light (4.41) suggests that the photothermal effect promotes the active sites of the NiS_x@$NiFe(OH)_y$/NF electrode and thus enhances the OER activity (Fig. S13†). To further investigate the OER stability, the *J*–*T* curves of NiS_x@$NiFe(OH)_y$/NF under NIR light were tested at 1.6 V *vs.* RHE for 8 h. As shown in Fig. 4d and Fig. S14,† NiS_x@$NiFe(OH)_y$/NF under NIR light illumination has increased OER activity, and its stability changes negligibly with respect to NiS_x@$NiFe(OH)_y$/NF without NIR light. NiS_x@$NiFe(OH)_y$/NF produced oxygen at a faster rate (0.58 mmol h^{-1}) with NIR light than NiS_x@$NiFe(OH)_y$/NF without NIR light (0.44 mmol h^{-1}) (Table S3†). As shown in Fig. S15,† the XRD patterns of NiS_x@$NiFe(OH)_y$/NF before and after NIR light irradiation test were consistent with that of the original NiS_x@$NiFe(OH)_y$/NF sample, indicating that there is no other crystalline material generation. In addition, the O_2 generation rates on NiS_x@$NiFe(OH)_y$/NF under and without NIR light irradiation are more clearly illustrated in ESI Video 1.†

Subsequently, we systematically investigated the origin of the enhanced OER kinetics and activity of NiS_x@$NiFe(OH)_y$/NF under near-infrared light irradiation. As mentioned before, the OER is a classical nonhomogeneous reaction, in which reaction rate dependence on the temperature can be deduced from

the Arrhenius equation. The temperature variations and thermal imaging pictures of NiS_x@$NiFe(OH)_y$/NF and $NiFe(OH)_y$/NF in 1.0 M KOH solution under NIR light are shown in Fig. 5a. It is obvious that NiS_x@$NiFe(OH)_y$/NF after the same time of NIR light irradiation has a higher electrode temperature than $NiFe(OH)_y$/NF. Moreover, the negligible temperature change of the electrolyte (1.0 M KOH) excludes the effect of near-infrared light on the electrolyte. As shown in Fig. 5b, the UV-Vis-NIR absorption spectra show that NiS_x@$NiFe(OH)_y$/NF has a higher light absorption capacity than $NiFe(OH)_y$/NF and NF, which contributes significantly to its photo-thermal ability and is in agreement with the temperature test shown in Fig. 5a. Furthermore, as shown in Fig. 5c, under NIR light, the current response of NiS_x/NF (2.86 mA cm^{-2}) is larger than that of $NiFe(OH)_y$/NF (2.09 mA cm^{-2}) and is close to that of NiS_x@$NiFe(OH)_y$/NF (3.15 mA cm^{-2}). As shown in Fig. S16 and S17,† NiS_x/NF under NIR light irradiation has a greater ECSA change than $NiFe(OH)_y$/NF under NIR light irradiation, which further indicates that NiS_x/NF has a stronger photothermal response than $NiFe(OH)_y$/NF. From the above discussion, it can be suggested that the photothermal effect of NiS_x is the main reason for the increase of current response of NiS_x@$NiFe(OH)_y$/NF.

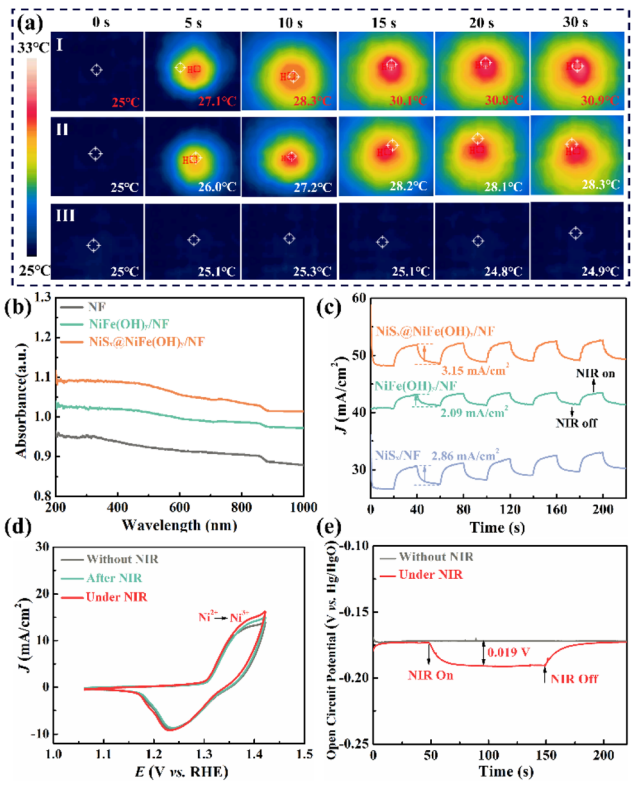

Fig. 5 (a) Thermal imaging pictures of I: NiS_x@$NiFe(OH)_y$/NF and II: $NiFe(OH)_y$/NF in 1.0 M KOH solution and III: 1.0 M KOH solution under NIR light irradiation. (b) UV-Vis absorption spectra of NF, $NiFe(OH)_y$/NF and NiS_x@$NiFe(OH)_y$/NF. (c) *J*–*T* curves at 1.6 V *vs.* RHE of NiS_x/NF, $NiFe(OH)_y$/NF and NiS_x@$NiFe(OH)_y$/NF. (d) CV curves of NiS_x@$NiFe(OH)_y$/NF before, under and after NIR light illumination. (e) Open circuit potential (OCP) of NiS_x@$NiFe(OH)_y$/NF with and without NIR light illumination.

Furthermore, some reports have found that the photothermal effect can promote the formation of a micro-electric field at the electrode.[52] To verify that possibility, the CV curves of NiS_x@$NiFe(OH)_y$/NF before, after and under NIR light illumination were first measured. As shown in Fig. 5d, upon irradiation with near-infrared light, NiS_x@$NiFe(OH)_y$/NF has an enhanced oxidation peak, which is consistent with the previous observation that the photothermal effect accelerates the OER kinetics with the promotion of more reactive active site generation ($Ni^{2+} \rightarrow Ni^{3+}$). Furthermore, after NIR irradiation, the enhanced oxidation peak still appeared in the CV curve, suggesting that the photothermal effect can promote the redistribution of the surface charge of NiS_x@$NiFe(OH)_y$/NF and generate more active Ni^{3+} sites. As shown in Fig. S18,† it is noteworthy that the peak area ratio of Ni^{3+} in Ni 2p in high-resolution XPS increased from 19.6% (before NIR light irradiation) to 35.3% (after NIR light irradiation), while the peak area ratio of Ni^{2+} in Ni 2p in high-resolution XPS decreased from 52.8% (before NIR light irradiation) to 43.9% (after NIR light irradiation), which further suggested the rearrangement of the surface charge in NiS_x@$NiFe(OH)_y$/NF. In addition, the open circuit potential (OCP) of NiS_x@$NiFe(OH)_y$/NF in the absence and presence of NIR light irradiation demonstrates variations in the surface electric field.[43] As shown in Fig. 5e, the open-circuit potential variation of NiS_x@$NiFe(OH)_y$/NF before and after NIR light irradiation is 0.019 V, which further indicates that the photothermal effect can promote the formation of a micro-electric field in NiS_x@$NiFe(OH)_y$/NF.

4. Conclusions

In summary, we demonstrated that the photothermal effect and its induced micro-electric field can significantly improve the thermodynamic and kinetics properties of the electrocatalytic OER on NiS_x@$NiFe(OH)_y$/NF. NiS_x@$NiFe(OH)_y$/NF has an obvious heterojunction effect and can effectively absorb NIR light, which together improve the OER performance of NiS_x@$NiFe(OH)_y$/NF. It is noteworthy that due to the photothermal effect and the induced micro-electric field, the OER performance of NiS_x@$NiFe(OH)_y$/NF is significantly enhanced. Compared with no NIR light irradiation, the overpotential at 50 mA cm^{-2} and the Tafel slope of NiS_x@$NiFe(OH)_y$/NF under NIR light irradiation were 234.1 mV and 38.0 mV dec^{-1}, which were lower by 12.4 mV and 7.1 mV dec^{-1}, respectively. Furthermore, NiS_x@$NiFe(OH)_y$/NF under NIR irradiation was able to operate consistently at 1.6 V *vs.* RHE for 8 h with 99% activity maintained. This work provides inspiration for enhancing the thermodynamics and kinetics of electrocatalysts for the OER.

Conflicts of interest

The authors declare no competing financial interest.

Acknowledgements

This work was supported by the National Natural Science Foundation of China (22005254, 41702037, 52302220 and 52373087), the Natural Science Foundation of Sichuan Province (2023NSFSC1128), the Natural Science Foundation of Chongqing (2023NSCQ-MSX0210), the Project of Innovation Training Program for College Students in Sichuan Province (S202310619089), the Project of Southwest University of Science and Technology (20zx7142), and the Graduate Science and Technology Innovation Training Program Project of Chongqing University of Science and Technology (YKJCX2220202 and YKJCX2220520).

Notes and references

1 Z. W. Seh, J. Kibsgaard, C. F. Dickens, I. Chorkendorff, J. K. Norskov and T. F. Jaramillo, *Science*, 2017, **355**, eaad4998.
2 P. De Luna, C. Hahn, D. Higgins, S. A. Jaffer, T. F. Jaramillo and E. H. Sargent, *Science*, 2019, **364**, eaav3506.
3 Y. Luo, Z. Zhang, M. Chhowalla and B. Liu, *Adv. Mater.*, 2022, **34**, 2201486.
4 J. T. Ren, L. Chen, H. Y. Wang, W. W. Tian and Z. Y. Yuan, *Energy Environ. Sci.*, 2024, **17**, 49–113.
5 Q. Hu, J. Hou, Y. Liu, L. Li, Q. Ran, J. Mao, X. Liu, J. Zhao and H. Pang, *Adv. Mater.*, 2023, **35**, 2303336.
6 Z. Y. Yu, Y. Duan, X. Y. Feng, X. Yu, M. R. Gao and S. H. Yu, *Adv. Mater.*, 2021, **33**, e2007100.
7 J. Zhao, J. J. Zhang, Z. Y. Li and X. H. Bu, *Small*, 2020, **16**, 2003916.
8 T. Zhao, Y. Wang, S. Karuturi, K. Catchpole, Q. Zhang and C. Zhao, *Carbon Energy*, 2020, **2**, 582–613.
9 Y. Wang, J. Mi and Z. S. Wu, *Chem Catal.*, 2022, **2**, 1624–1656.
10 M. Yu, E. Budiyanto and H. Tuysuz, *Angew. Chem., Int. Ed.*, 2022, **61**, e202103824.
11 X. Xie, L. Du, L. Yan, S. Park, Y. Qiu, J. Sokolowski, W. Wang and Y. Shao, *Adv. Funct. Mater.*, 2022, **32**, 2110036.
12 H. Ding, H. Liu, W. Chu, C. Wu and Y. Xie, *Chem. Rev.*, 2021, **121**, 13174–13212.
13 Q. Shi, C. Zhu, D. Du and Y. Lin, *Chem. Soc. Rev.*, 2019, **48**, 3181–3192.
14 F. Gao, Y. Zhang, Z. Wu, H. You and Y. Du, *Coord. Chem. Rev.*, 2021, **436**, 213825.
15 Y. Zhao, J. You, L. Wang, W. Bao and R. Yao, *Int. J. Hydrogen Energy*, 2021, **46**, 39146–39182.
16 X. Wang, H. Zhong, S. Xi, W. S. V. Lee and J. Xue, *Adv. Mater.*, 2022, **34**, 2107956.
17 V. Vij, S. Sultan, A. M. Harzandi, A. Meena, J. N. Tiwari, W. G. Lee, T. Yoon and K. S. Kim, *ACS Catal.*, 2017, **7**, 7196–7225.
18 X. Cui, M. Wu, X. Liu, B. He, Y. Zhu, Y. Jiang and Y. Yang, *Chem. Soc. Rev.*, 2024, **53**, 1447–1494.
19 Z. P. Wu, X. F. Lu, S. Q. Zang and X. W. Lou, *Adv. Funct. Mater.*, 2020, **30**, 1910274.
20 A. Wang, Z. Zhao, D. Hu, J. Niu, M. Zhang, K. Yan and G. Lu, *Nanoscale*, 2019, **11**, 426–430.
21 K. Zhu, X. Zhu and W. Yang, *Angew. Chem., Int. Ed.*, 2018, **58**, 1252–1265.
22 J. Mohammed-Ibrahim, *J. Power Sources*, 2020, **448**, 227375.
23 R. Zhang, A. Xie, L. Cheng, Z. Bai, Y. Tang and P. Wan, *Chem. Commun.*, 2023, **59**, 8205–8221.
24 M. Liu, K. A. Min, B. Han and L. Y. S. Lee, *Adv. Energy Mater.*, 2021, **11**, 2101281.
25 L. Gong, H. Yang, A. I. Douka, Y. Yan and B. Y. Xia, *Adv. Sustainable Syst.*, 2020, **5**, 2000136.
26 D. Drevon, M. Görlin, P. Chernev, L. Xi, H. Dau and K. M. Lange, *Sci. Rep.*, 2019, **9**, 1532.
27 A. J. Bard and L. R. Faulkner, *Electrochemical methods: fundamentals and applications*, John Wiley & Sons Inc., New York, 2000.
28 M. Menzinger and R. Wolfgang, *Angew. Chem., Int. Ed. Engl.*, 1969, **8**, 438–444.
29 T. Guo, L. Li and Z. Wang, *Adv. Energy Mater.*, 2022, **12**, 2200827.
30 X. Li, X. Hao, A. Abudula and G. Guan, *J. Mater. Chem. A*, 2016, **4**, 11973–12000.
31 S. Anantharaj and S. Noda, *Small*, 2020, **16**, e1905779.
32 J. S. Kim, B. Kim, H. Kim and K. Kang, *Adv. Energy Mater.*, 2018, **8**, 1702774.
33 D. Zhou, S. Wang, Y. Jia, X. Xiong, H. Yang, S. Liu, J. Tang, J. Zhang, D. Liu, L. Zheng, Y. Kuang, X. Sun and B. Liu, *Angew. Chem., Int. Ed.*, 2018, **58**, 736–740.
34 J. Zhang, J. Qian, J. Ran, P. Xi, L. Yang and D. Gao, *ACS Catal.*, 2020, **10**, 12376–12384.
35 F. Duan, Y. Huang, T. Han, B. Jia, X. Zhou, Y. Zhou, Y. Yang, X. Wei, G. Ke and H. He, *Inorg. Chem.*, 2023, **62**, 12119–12129.
36 Y. Li, X. Li, X. T. Wang, L. J. Jian, N. I. M. Abdallah, X. F. Dong and C. W. Wang, *Colloids Surf., A*, 2021, **608**, 125565.
37 B. Jin, Y. Li, J. Wang, F. Meng, S. Cao, B. He, S. Jia, Y. Wang, Z. Li and X. Liu, *Small*, 2019, **15**, e1903847.
38 J. Yao, W. Huang, W. Fang, M. Kuang, N. Jia, H. Ren, D. Liu, C. Lv, C. Liu, J. Xu and Q. Yan, *Small Methods*, 2020, **4**, 2000494.
39 L. Gao, X. Cui, Z. Wang, C. D. Sewell, Z. Li, S. Liang, M. Zhang, J. Li, Y. Hu and Z. Lin, *Proc. Natl. Acad. Sci. U. S. A.*, 2021, **118**, e2023421118.
40 H. J. Niu, Y. Yan, S. Jiang, T. Liu, T. Sun, W. Zhou, L. Guo and J. Li, *ACS Nano*, 2022, **16**, 11049–11058.
41 Y. Chang, Z. Ma, X. Lu, S. Wang, J. Bao, Y. Liu and C. Ma, *Angew. Chem., Int. Ed.*, 2023, **62**, e202310163.
42 S. R. Logan, *J. Chem. Educ.*, 1982, **59**, 279–281.
43 Z. Wang, Y. Wang, Y. Zhang, X. Sun, Y. Lou, Y. Zhang, Y. Dong, C. Pan and Y. Zhu, *Appl. Catal., B*, 2022, **313**, 121452.
44 Y. Zhang, Y. Wang, H. Jiang and M. Huang, *Small*, 2020, **16**, e2002550.
45 B. Zhang, H. Luo, B. Ai, Q. Gou, J. Deng, J. Wang, Y. Zheng, J. Xiao and M. Li, *Small*, 2022, **19**, 2205431.

46 L. Yang, H. Li, Y. Yu, Y. Wu and L. Zhang, *Appl. Catal., B*, 2020, **271**, 118939.
47 A. K. Díaz-Duran, G. Iadarola-Pérez, E. B. Halac and F. Roncaroli, *Top. Catal.*, 2022, **65**, 887–901.
48 Z. Zhao, X. Wang, S. Tang, M. Cheng and Z. Shao, *Int. J. Hydrogen Energy*, 2021, **46**, 25332–25340.
49 A. Wang, H. Li, J. Xiao, Y. Lu, M. Zhang, K. Hu and K. Yan, *ACS Sustainable Chem. Eng.*, 2018, **6**, 15995–16000.
50 M. Chen, N. Kitiphatpiboon, C. Feng, Q. Zhao, A. Abudula, Y. Ma, K. Yan and G. Guan, *Appl. Catal., B*, 2023, **330**, 122577.
51 F. Du, L. Shi, Y. Zhang, T. Li, J. Wang, G. Wen, A. Alsaedi, T. Hayat, Y. Zhou and Z. Zou, *Appl. Catal., B*, 2019, **253**, 246–252.
52 Y. Gutiérrez, M. Losurdo, F. González, H. O. Everitt and F. Moreno, *J. Phys. Chem. C*, 2020, **124**, 7386–7395.